

Cite this: *Nanoscale*, 2019, **11**, 21364

# Thermally reduced fluorographenes as efficient electrode materials for supercapacitors†

Martin Petr,<sup>a</sup> Petr Jakubec,<sup>a\*</sup> Václav Ranc,<sup>b</sup> Veronika Šedajová,<sup>b</sup> Rostislav Langer,<sup>b</sup> Miroslav Medved,<sup>b</sup> Piotr Błoński,<sup>b</sup> Josef Kašlík,<sup>b</sup> Vojtěch Kupka,<sup>b</sup> Michal Otyepka<sup>b\*</sup> and Radek Zbořil<sup>b</sup>

There is an urgent need for a simple and up-scalable method for the preparation of supercapacitor electrode materials due to increasing global energy consumption worldwide. We have discovered that fluorographene exhibits great potential for the development of new kinds of supercapacitors aimed at practical applications. We have shown that time control of isothermal reduction of fluorographite at 450 °C under a hydrogen atmosphere led to the fine-tuning of fluorine content and electronic properties of the resulting fluorographene derivatives. Charge transfer resistances ( $R_{ct}$ ) of the thermally reduced fluorographenes (TRFGs) were decreased with respect to the pristine fluorographene; however, the  $R_{ct}$  vs. time-of-reduction plot showed a v-shaped profile. The specific capacitance vs. time-of-reduction of TRFG followed the v-shaped trend, which could be the result of the decreasing content of  $sp^3$  carbons and increasing content of structural defects. An optimized material exhibited values of specific capacitance up to 539 F g<sup>-1</sup> recorded at a current density of 0.25 A g<sup>-1</sup> and excellent cycling durability with 100% specific capacitance retention after 1500 cycles in a three-electrode configuration and 96.7% of specific capacitance after 30 000 cycles in a two-electrode setup.

Received 22nd August 2019,  
Accepted 17th September 2019

DOI: 10.1039/c9nr07255a

rsc.li/nanoscale

## Introduction

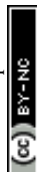
Considering the significant increase in world population and its reliance on energy-based devices, we assume that global energy consumption will significantly rise. It has been estimated that the demand for energy resources will have increased by 100% by the year 2050.<sup>1,2</sup> When we take into account that fossil fuel resources are strictly limited, it is understandable that research focused on sustainable energy resources coupled with suitable energy storage technologies attracts intense interest. Supercapacitors belong to the group of energy storage devices that display significant advantages such as high-power density, long cycle life, and a small size when compared to batteries or fuel cells.<sup>3</sup> They can store more energy than classical conventional capacitors while preserving

a similar cell construction. However, the energy stored in supercapacitors (SCs) is about one order of magnitude lower than that of batteries. As the energy density ( $E$ ) is related to capacitance ( $C$ ) and voltage window ( $V$ ) by the equation  $E = \frac{1}{2}CV^2$ , it can be concluded that  $E$  can be increased by increasing one or both terms.<sup>4</sup> The voltage range can be enhanced by employing organic electrolytes or ionic liquids instead of aqueous electrolytes (due to the thermodynamic stability of water beyond 1.23 V).<sup>5</sup> However, both kinds of electrolytes usually combine unfavourable properties such as low flash point, high-volatility, low electrical conductivity or low ionic conductivity at room temperature and, last but not least, toxicity and high cost. Moreover, a few ppm of water can significantly decrease the voltage window,<sup>6</sup> which imposes high demands on cell construction. The energy density also depends on the material used for the electrode. In general, all materials can be sorted into two basic groups.<sup>7</sup> The first group is represented by faradaic materials with redox active components which store charge *via* a fast and reversible faradaic reaction (pseudo-capacitive effect).<sup>8</sup> It has been reported several times before that materials such as transition metal oxides,<sup>9–12</sup> conductive polymers,<sup>13,14</sup> or their composites<sup>15</sup> rank among the typical examples. Conducting polymers possess many advantages such as low cost, high-conductivity in a doped state, and broad voltage window. However, swelling and shrinking of polymers represent a major problem leading

<sup>a</sup>Regional Centre for Advanced Technologies and Materials, Department of Experimental Physics, Faculty of Science, Palacký University Olomouc, 17. listopadu 1192/12, 771 46 Olomouc, Czech Republic

<sup>b</sup>Regional Centre for Advanced Technologies and Materials, Department of Physical Chemistry, Faculty of Science, Palacký University Olomouc, 17. listopadu 1192/12, 771 46 Olomouc, Czech Republic. E-mail: p.jakubec@upol.cz, michal.otyepka@upol.cz

†Electronic supplementary information (ESI) available: BET analysis, The plot of  $\log i$  vs.  $\log \nu$  of the FG-20H sample, HR-XPS spectra of C 1s derived from FG-12H and FG-24H samples, LED diode + life-time stability test, theoretical calculations. See DOI: 10.1039/c9nr07255a



to the mechanical degradation of materials, which results in hindering the electrochemical performance during testing.<sup>5</sup> Pseudo-capacitive materials such as  $\text{MnO}_2$  enable to enhance the specific capacitance over  $1000 \text{ F g}^{-1}$ , but they usually suffer from low electrical conductivity and compatibility with organic electrolytes.<sup>16,17</sup> Short cycling ability limited their practical application as well. The other group is electro-chemical double-layer capacitors (EDLCs) which store energy electrostatically *via* a reversible ion absorption/desorption process at the electrode/electrolyte interface. Conway reported that an optimal material for an EDLC supercapacitor must have three key parameters as follows: (1) high specific area, (2) good intra- and interparticle conductivity in porous systems, and (3) good electrolyte accessibility to the intrapore space.<sup>18</sup> Generally, carbon-based materials such as activated carbon,<sup>19–21</sup> carbon nanotubes,<sup>22,23</sup> carbon nanofibers,<sup>24,25</sup> templated porous carbons,<sup>26</sup> carbon aerogels<sup>27–31</sup> and carbide-derived carbons<sup>32–34</sup> are able to meet these requirements. However, a major part of these materials possess values of specific capacitance only in the range of  $75\text{--}175 \text{ F g}^{-1}$ .<sup>7</sup> Graphene, a two-dimensional carbon material, exhibits prominent intrinsic chemical and physical properties such as excellent electrical and thermal conductivity, mechanical strength, and large surface area.<sup>35</sup> On the basis of these findings, it has been proposed that graphene can be used as a competitive material for SCs.<sup>36</sup> Despite the above-mentioned qualities, graphene sheets exhibit strong inertness to chemical reactions<sup>37</sup> and are prone to restacking, which reduces their usability in the field of supercapacitors.<sup>38</sup> Therefore, considerable scientific effort has been devoted to strategies to overcome these limitations. This may involve managed changes of morphology during the synthesis of graphene sheets including for instance the creation of different porous 3D structures.<sup>39–41</sup> Different ways to boost the capacitance include also the formation of various graphene composites,<sup>42</sup> doping of graphene with heteroatoms,<sup>43–45</sup> application of metal oxides<sup>11,46–48</sup> or metal-organic frameworks,<sup>49–54</sup> and functionalization of graphene sheets with different molecules through both covalent and non-covalent interactions.<sup>55–57</sup> Halogenation of graphite represents an interesting approach to create few-layer graphene-like structures with extraordinary electrochemical properties.<sup>58</sup> For instance, the intercalation of bromine, chlorine and fluorine atoms significantly improves the delamination process and endows the materials with a significantly higher surface area.<sup>59–61</sup> Beyond these benefits, it has been also reported that the doping of halogen atoms highly affects the electronic properties such as conductivity.<sup>62–65</sup> An *et al.* prepared an optimized fluorinated graphene hydrogel with capacitance values up to  $227 \text{ F g}^{-1}$  at a current density of  $1 \text{ A g}^{-1}$  in  $6 \text{ M KOH}$ .<sup>66</sup> Kou *et al.* synthesized a graphene based material (OMG-Cl) doped by chlorine giving the capacitance value of  $250 \text{ F g}^{-1}$  at a current density of  $0.5 \text{ A g}^{-1}$  in  $1 \text{ M H}_2\text{SO}_4$  and  $220 \text{ F g}^{-1}$  in  $6 \text{ M KOH}$ . The high capacitive performance was explained by an additional fast faradaic reaction induced from Cl-doping species.<sup>63</sup> Kakaei *et al.* reported chlorine-doped reduced graphene oxide nanosheets, which exhibited the capacitance

value of  $178.4 \text{ F g}^{-1}$  at a current density of  $1 \text{ A g}^{-1}$  in  $1 \text{ M H}_2\text{SO}_4$ .<sup>64</sup> Ye *et al.* described the fluffy reduced graphene oxide film doped with iodine with the capacitance of  $238 \text{ F g}^{-1}$  at a current density of  $0.5 \text{ A g}^{-1}$  in  $1 \text{ M H}_2\text{SO}_4$ .<sup>65</sup> Bulusheva *et al.* analyzed the structure and supercapacitor performance of graphene materials obtained from brominated and fluorinated graphites and concluded that the capacitance of a material doped with fluorine increased up to  $158 \text{ F g}^{-1}$  at a scan rate of  $2 \text{ mV s}^{-1}$  (in  $1 \text{ M H}_2\text{SO}_4$ ).<sup>67</sup>

Herein, we report a simple and up-scalable method for the preparation of partially fluorinated graphene derivatives based on thermal reduction of a fully fluorinated sample employing a reducing hydrogen gas. We have shown that the capacitance is influenced by the number of fluorine atoms as well as the hydrogenation process. An optimized material exhibits values of specific capacitance up to  $539 \text{ F g}^{-1}$  recorded at a current density of  $0.25 \text{ A g}^{-1}$ . This capacitor system can be cycled reversibly in the voltage range of  $0.1\text{--}0.6 \text{ V}$  and exhibits excellent cycling durability, with 100% specific capacitance retention after 1500 cycles in a three-electrode configuration and 96.7% specific capacitance after 30 000 cycles in a two-electrode setup. Moreover, the evolution of structural changes and related electronic properties is explained in detail using both experimental and theoretical approaches. The environmentally friendly nature of our derivatives (one-step synthesis without any presence of heavy metals, neutral character of the electrolyte) holds great potential in developing new kinds of supercapacitors for practical applications.

## Experimental

### Microscopy techniques

A Hitachi SU6600 scanning electron microscope (SEM) equipped with a field emission gun (FEG) and transmission electron microscope JEOL JEM 2100 operating at  $200 \text{ kV}$  (TEM) were used for morphology investigation. High-resolution TEM images including STEM-HAADF (high-angle annular dark-field imaging) analyses for elemental mapping of the products were performed with an FEI Titan HRTEM (high-resolution TEM) microscope operating at  $200 \text{ kV}$ . For these analyses, a droplet of the dispersion of the material in DMF at a concentration of  $\sim 0.1 \text{ mg mL}^{-1}$  was deposited onto a carbon-coated copper grid and dried. AFM images were obtained using the NTegra Spectra instrument (NT-MDT, Russia) in the tapping mode using NSG30 probes. In total,  $5 \mu\text{L}$  of the ethanolic dispersion ( $c = 1 \text{ mg L}^{-1}$ ) of the analyzed nanomaterial was deposited on a  $\text{SiO}_2$  wafer and left to dry for 30 minutes. The sample was measured immediately after that.

### Raman

Raman data were measured on a DXR Raman spectrometer (Thermo Scientific, USA) with a laser operating at  $633 \text{ nm}$ . The sample ( $0.1 \text{ mg}$ ) was deposited on a silicon wafer ( $1 \times 1 \text{ cm}$ ) and an excitation laser was focused on its surface. The laser power on the sample was set to  $2 \text{ mW}$ , and the exposition time



was 3 s. Each measured Raman spectrum was an average of 512 experimental microscans. Raman spectra were processed using control software (Omnic, version 8, Thermo Scientific, USA).

### XPS

The XPS measurements were carried out with the PHI 5000 VersaProbe II XPS system (Physical Electronics) with a monochromatic Al-K $\alpha$  source (15 kV, 50 W) and photon energy of 1486.7 eV. All spectra were recorded in a vacuum of  $1.2 \times 10^{-7}$  Pa at a room temperature of 20 °C. The analyzed area of the sample was a spot of 200  $\mu$ m in diameter. The survey spectra were recorded at a pass energy of 187.850 eV with an electron-volt step of 0.8 eV; the high-resolution spectra were recorded at a pass energy of 23.500 eV with an electron-volt step of 0.2 eV. Dual beam charge compensation was used for all measurements. The spectra were evaluated with the MultiPak (Ulvac - PHI, Inc.) software. All binding energy (BE) values were referenced to the carbon peak C 1s at 284.80 eV.

### BET

The surface area and pore size analysis of GF powders was performed by means of N<sub>2</sub> adsorption/desorption measurements at 77 K on a volumetric gas adsorption analyzer (3Flex, Micromeritics, USA) up to 0.965  $P/P_0$ . Prior to the analysis, the samples were degassed under high vacuum ( $10^{-4}$  Pa) at 130 °C for 12 hours while high purity (99.999%) N<sub>2</sub> and He gases were used for the measurements. The Brunauer-Emmett-Teller area (BET) was determined with respect to Rouquerol criteria for BET determination<sup>68</sup> assuming a molecular cross-sectional area of 16.2 Å<sup>2</sup> for N<sub>2</sub> (77 K). Pore size distribution was analyzed by the N<sub>2</sub>-DFT slit pore kernel.

### Electrochemical methods

The electrochemical analyzer PGSTAT 128N (Eco-Chemie, The Netherlands) using software package NOVA 1.11.2 was used for performing electrochemical experiments including cyclic voltammetry, galvanostatic charge-discharge characteristics, and electrochemical impedance spectroscopy. A three-electrode system was used as a proof-of-concept in order to collect all information about the electrochemical performance of the fluorographene samples. Following this set-up, a glassy carbon electrode (GCE) was used as a working electrode, a platinum electrode served as the counter electrode, and a Ag/AgCl electrode was used as the reference electrode, respectively. The GCE electrodes were modified with the samples applying a drop-coating technique as follows: a 10  $\mu$ L drop of a powder suspension (0.2 g L<sup>-1</sup>) was coated onto the surface of the GCE electrode and allowed to dry at ambient temperature to form a thin film. Electrochemical impedance spectroscopy (EIS) measurements were performed by applying an AC voltage with a 5 mV amplitude over a frequency range 0.1 Hz to 10 kHz at the open circuit potential (OCP). All the obtained data were fitted using a modified Randles circuit. Sodium sulphate (Na<sub>2</sub>SO<sub>4</sub>;  $c = 1$  mol L<sup>-1</sup>) was used as the electrolyte in all experiments. The gravimetric capacitance for the three-electrode

system was calculated both from cyclic voltammograms and galvanostatic charge/discharge curves as follows:

$$C_m = \frac{\int_{\nu_i}^{\nu_f} i dV}{\nu \times \Delta V \times m}$$

$$C_m = \frac{I \times \Delta t}{m \times \Delta V}$$

where  $C_m$  is the gravimetric capacitance of the electrode (F g<sup>-1</sup>),  $\int i dV$  is the voltammetric charge obtained by the integration of the area under the reverse peak of the cyclic voltammogram,  $\nu$  is the scan rate (V s<sup>-1</sup>),  $\Delta V$  is the potential window,  $m$  is the mass of the material deposited on the working electrode,  $I$  is the discharge current (A), and  $t$  is the discharge time (s).

A symmetrical supercapacitor device (EL-CELL, GmbH, Germany) was used to test the cycling stability of the FG-20H sample. Briefly, an active material without any additives (for instance binders, carbon black *etc.*) was dispersed in ultrapure water ( $\approx 4$  mg ml<sup>-1</sup>) and sonicated for 1 hour. Then, 400  $\mu$ L of dispersion was drop-coated on the surface of the gold disc electrode and dried under an *infra* lamp to achieve a mass loading of at least 2 mg cm<sup>-2</sup>. For the assembly of the supercapacitor device, two gold disc electrodes with the same loading of the active material were placed in a plastic sleeve (El-Cell sleeves with the Whatman® glass microfiber membrane). The separator membrane was soaked with 100  $\mu$ L of the electrolyte. Stainless steel plungers were used to press the electrodes and the whole device was tightened and connected.

### Computational methods

The first-principles calculations were performed by applying the spin-polarized density functional theory (SDFT) with the Perdew, Burke, and Ernzerhof (PBE)<sup>69</sup> exchange and correlation functional and projected augmented wave potentials (PAW), as implemented in the Vienna *ab initio* simulation package (VASP).<sup>70–73</sup> The wave functions were expanded in the plane-wave basis set with a minimum cutoff of 400 eV. The Brillouin zone integrations were performed with  $6 \times 6 \times 1$  (structure and cell optimization)  $\Gamma$ -centered Monkhorst-Pack  $k$ -point mesh<sup>74</sup> per conventional  $3 \times 3$  triclinic cell containing 18 carbon atoms, with the larger  $6 \times 6$  triclinic cell containing 72 carbon atoms and the orthorhombic cell containing 48 ad-atoms. All optimized structures were converged to forces of less than  $10^{-2}$  eV Å<sup>-1</sup>, with a criterion  $10^{-6}$  eV for each SCF cycle.

The thermodynamic stability of graphene-based structures expressed as the averaged binding energy was calculated as:

$$E^b = \frac{1}{z} (E_{CX} - E_C - zE_X)$$

where  $E_{CX}$  is the energy of the optimized functionalized graphene model,  $E_C$  is the energy of optimized graphene,  $E_X$  is the energy of single fluorine or hydrogen ad-atoms, and  $z$  is the number of fluorine or hydrogen ad-atoms.

To evaluate the possibility of the formation of a specific arrangement on graphene, we calculated the Boltzmann





probability at 450 K of fifteen lowest-in-energy structures as follows:

$$p_i = \frac{e^{-\frac{E_i^T}{k_B T}}}{Q}$$

where the partition function  $Q$  is expressed as:

$$Q = \sum_j e^{-\frac{E_j^T}{k_B T}}$$

where  $p_i$  is the probability of the  $i$ -th configuration,  $E_i^T$  is its total energy per computational cell (the summation runs over all considered configurations),  $k_B$  is the Boltzmann constant, and  $T$  is the thermodynamic temperature.

## Reagents

Fluorinated graphite polymer (>61 wt% F) and sodium sulfate ( $\text{Na}_2\text{SO}_4$ , 99% purity) were purchased from Sigma-Aldrich (Czech Republic). Milli-Q Water (MQ water, 18.3 M $\Omega$ , Millipore Corp., Milford, MA, USA) was used for the preparation of all electrolyte solutions.

## Synthesis of fluorographene derivatives

Defluorination was performed by isothermal annealing of approximately 25 mg of the precursor (fluorinated graphite polymer (>61 wt% F)) at a temperature of 450 °C (heating ramp 15 °C min<sup>-1</sup>) under continuous flushing of the reaction chamber XRK 900 mounted to an X-ray diffractometer  $\dot{\lambda}$ Pert PRO MPD with pure hydrogen gas (6.0) with flow rate 40 mL min<sup>-1</sup> and relative overpressure 1 bar for a time period ranging from 12 to 24 hours. The temperature of 450 °C was selected as the most suitable temperature for the continuous defluorination process.

## Results and discussion

Complex characterization of the prepared samples was performed in order to understand the electrochemical properties of fluorographene derivatives in detail. The morphology of the precursor and the samples labelled as FG-20H and FG-20Ham was evaluated by both SEM and TEM. The SEM image of the precursor (Fig. 1a) shows a typical graphite-like structure as expected. On the other hand the material thermally treated under a hydrogen atmosphere for 20 hours (FG-20H sample) consisted of thin and almost transparent flakes with a lateral size up to 2  $\mu\text{m}$  as shown in Fig. 1b. Interestingly, a similar few-layer structure was also observed for the sample collected after the cycling stability measurement (Fig. 1c; FG-20Ham). The TEM images perfectly reflect the results obtained by the SEM measurement. The selected area electron diffraction (SAED) patterns confirmed the amorphous nature of all samples. Moreover, the occurrence of the same sharp rings for both FG-20H and FG-20Ham samples confirms the fact that the sample does not undergo any significant changes during the stability measurement (insets of Fig. 1e and f). High-



**Fig. 1** (a–c) SEM and (d–f) TEM images of the FG sample, FG-20H and FG-20Ham samples (FG-20Ham: sample collected after the cycling stability measurement; inset: SAED patterns of the abovementioned samples). (g, h) HRTEM micrographs of the FG-20H sample. (i) Darkfield HRTEM image used for EDS chemical mapping. (j) EDS chemical mapping of carbon, nitrogen, oxygen, and fluorine; (k) EDAX spectrum of the FG-20H sample. (l) AFM image of the FG-20H sample; inset: height profile of the FG-20H sample. All scale-bars were unified from a graphical point-of-view in order to provide better visibility.

resolution TEM (HRTEM) confirmed a thin layer structure of the FG-20H sample with the same size as previously described by SEM imaging (Fig. 1g–i). Moreover, EDS elemental mapping revealed that the elements such as oxygen, nitrogen, carbon, and fluorine were homogeneously distributed over the surface (Fig. 1j). It is worth noting that the presence of hydrogen adatoms cannot be excluded because of the reducing reaction conditions. The EDAX spectrum of the FG-20H sample is shown in Fig. 1k. All the obtained microscopy data suggested that the thickness of the FG-20 sample was in units of nm. The AFM image (Fig. 1l) and the corresponding height-profile (inset of Fig. 1l) scan showed that the thickness of the flakes ranged from 1.0 to 1.9 nm, indicating only few-layer structures.

While microscopy techniques can be regarded as very local evaluation methods, Raman scattering can be used to estimate an average number of layers in graphene-based materials as well as the number and origin of defects.<sup>75,76</sup> The D peak is related to the presence of atomic scale defects including the  $\text{sp}^3$  carbon atoms; the G peak is connected to the first order scattering of the stretching vibration mode  $E_{2g}$ , which is typical of the  $\text{sp}^2$  carbon domains.<sup>77</sup> The ratio of D to G bands ( $I_D/I_G$ ) can serve as a tool for the characterization of defects in graphene-based materials.<sup>78</sup> While the FG-12H sample exhibits a  $I_D/I_G$  ratio of 1.14, the FG-20H sample gives the  $I_D/I_G$  value of



0.87, indicating an increased content of  $sp^2$  hybridized carbon atoms (Fig. 2a and b). Conversely, the FG-24H sample exhibits the ratio of  $I_D/I_G$  around 1.05, indicating an increasing number of atomic scale defects accompanied by the disruption of  $\pi$ -conjugated domains (Fig. 2c). A small upshift of the D band from  $1363\text{ cm}^{-1}$  to  $1332\text{ cm}^{-1}$  for FG-20H can be ascribed to the rearrangement or cleavage of C-ad-atom bonds. The non-monotonous evolution of the  $I_D/I_G$  ratio indicates the complexity of structural changes in the material that is also reflected in the time of reaction of its electrochemical properties (*vide infra*).

X-ray photoelectron spectroscopy (XPS) was conducted to provide a better insight into the composition of the TRFG samples. Table 1 shows that the content of fluorine drops significantly during the first 12 hours of the isothermal reduction. Then, roughly reaching constant values of 0.9% between 14 and 18 hours. It decreases again to 0.5% after 24 hours of reduction. Conversely, the relative content of carbon atoms exhibits an increasing trend. This phenomenon can be related to the rearrangement or cleavage of C-ad-atom bonds during the thermal decomposition of the FG samples. A similar trend was observed for the FG samples prepared at different temperatures<sup>79,80</sup> and also for the FG samples pre-

pared at a constant temperature but different pressures, as reported previously.<sup>81</sup>

Fig. 3a shows a survey spectrum of the FG-20H sample and its elemental composition (inset of Fig. 3a). The presence of the N 1s peak in the spectrum may be attributed to the presence of dimethylformamide, which was used as a solvent. The C 1s spectra were further fitted using a Gaussian function with a Shirley background correction. The deconvoluted C 1s XPS spectra of the FG-20H sample (Fig. 3b) show seven symmetric component peaks, corresponding to carbon atoms in different functional groups. The two first peaks located at 284.63 eV and 284.94 eV can be assigned to the  $sp^2$  C=C bond and  $sp^3$  C-C bond, respectively. It is possible to recognize that the peak intensity of the C=C bond in  $sp^2$  hybridization is higher with respect to the peak intensity of the C=C bond in  $sp^3$  hybridization. These findings along with the C 1s HR-XPS spectra for the FG-12H and the FG-24H samples (see Fig. S3†) are fully in line with the time evolution of the  $I_D/I_G$  ratio in Raman spectra. The peaks located at 286.01, 287.35, 290.36, and 291.74 eV were ascribed to C-C-F/C-O, C=O, C-F, and C-F<sub>2</sub> covalent bonds, respectively. The peak placed at 288.44 eV in the C 1s spectrum reflects partial transformation of the covalent C-F bond to the corresponding semi-ionic C-F bond.<sup>82</sup> This phenomenon can be related to the shift in the electron cloud of the covalent C-F bonds induced by the formation of H-bonds.<sup>83</sup> The BET measurement was used to evaluate the specific surface area (SSA) of different TRFG samples. Fig. S1a† depicts the N<sub>2</sub> adsorption-desorption isotherms recorded at 77 K as well as the density functional theory (DFT) calculations of the pore size distribution of the TRFG samples. According to IUPAC conventions, the shape of all isotherms can be assigned to the combination of type I and IV, which is typical of microporous and mesoporous structures, respectively. The presence of a narrow hysteresis loop indicates an open porous structure, where there is no significant delay in the capillary evaporation of nitrogen. The FG-12H sample exhibits a SSA of  $308\text{ m}^2\text{ g}^{-1}$ , while the FG-20H and FG-24H samples show a similar SSA of  $335\text{ m}^2\text{ g}^{-1}$ . A small increase in the BET surface area (at around 8%) can be related to the thermal decomposition of the samples prepared with a longer period of synthesis. The hierarchical pore distribution of all FG samples (Fig. S1b†) indicates the presence of micropores with the size of <1 nm and mesopores with the size ranging from 2 to 10 nm. While the content of the larger pores does not change significantly, the micropores become notably more abundant at the final phase of the reaction (24H), suggesting that the material undergoes severe structural changes such as the release of fragments and formation of vacancies.

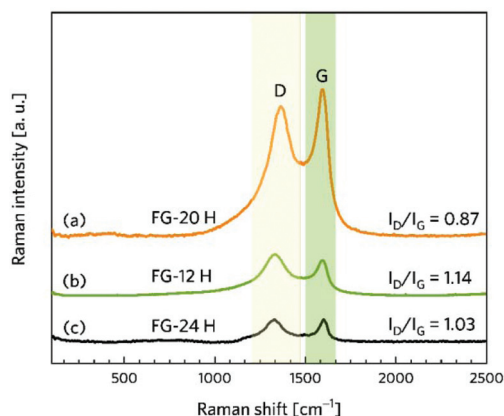


Fig. 2 Raman spectra of (a) FG-20H, (b) FG-12H, (c) and FG-24H samples and the corresponding intensity ratios  $I_D/I_G$ .

Table 1 Elemental composition of FG samples derived from XPS analyses

Time of synthesis (hours)	C 1s (atomic %)	O 1s	F 1s
Precursor	45.78	0.21	54.01
FG-2H	74.84	2.23	22.94
FG-12H	95.01	3.62	1.37
FG-14H	95.29	3.85	0.86
FG-16H	95.62	3.51	0.87
FG-18H	95.75	3.38	0.87
FG-20H	95.83	3.34	0.83
FG-22H	95.92	3.35	0.73
FG-24H	96.00	3.48	0.52

### Electrochemical performance of fluorographene derivatives

For testing the electrochemical performance of fluorographene derivatives at the electrode|electrolyte interface, both potential and current should be monitored. Hence, a three-electrode system using a reference electrode was selected as a more suitable system compared to the 2-electrode cell. An aqueous solution of 1 M sodium sulphate was used as an electrolyte. We





Fig. 3 (a) XPS survey and elemental analysis (inset) of the FG-20H sample. (b) HR-XPS spectra of C 1s from the FG-20H sample.

chose this neutral electrolyte because of its easy application involving work under open-air conditions, non-corrosive character, and environmentally friendly as well as relatively easily explainable charge-storage mechanism. Fig. 4a displays a scheme of fluorographene synthesis in a hydrogen-reducing atmosphere at a constant temperature of 450 °C. Fig. 4b shows a voltammetric response of the TRFG samples within the potential range of 0.1 to 0.6 V (scan rate of 50 mV s<sup>-1</sup>). The potential window between 0.1 and 0.6 V was selected as a stable region where no faradaic reaction occurred and where the contribution from the evolution of oxygen was negligible. As it is clearly evident, the process of defluorination signifi-

cantly enhances the current response (capacitance) of the TRFG derivatives as the time changes. We have observed that the maximum capacitance can be reached within 20 hours. After that, the electrochemical performance drops down to an almost constant value (Fig. 4c). We have also found that the shapes of all CV curves were approximately rectangular and exhibited a good symmetry, even at a high scan rate, which proves the excellent capacitive behaviour and rate performance, as shown in Fig. 4d. It is worth noting that the fully fluorinated graphene with one fluorine atom per carbon acts as a high-quality insulating material with a resistance higher than 10<sup>12</sup> Ω.<sup>84</sup> Partially fluorinated systems behave like semi-



Fig. 4 (a) Scheme of fluorographene synthesis. (b) CVs of GCEs modified with fluorographene samples recorded at a constant scan rate of 50 mV s<sup>-1</sup>. (c) Change of specific capacitance of FG samples with increasing time of synthesis. (d) CVs for the GCE modified with GF-20 H at different potential scan rates ranging from 10 to 200 mV s<sup>-1</sup>. (e) Variation of the b-value with the potential for the FG-20H sample.





conductors, whose bandgaps are highly dependent on the extent of fluorination.<sup>85</sup> Therefore, a decreasing capacitive performance after 20 hours of synthesis can be explained in terms of elemental composition as well as defect changes. When the FG sample undergoes thermal treatment at 450 °C in a reduction atmosphere of hydrogen gas, the ratio of F/C changes from 1.44 to 0.54, as it is evident from the XPS analysis. Once the amount of fluorine atoms decreases, the resistivity decreases as well, to the point (20 hours of the synthesis) when another defluorination process has no significant effect on lowering the resistivity. A further increase in the resistivity could be related to the increasing C—C vs. C—F ratio, which changes the type of defect responsible for the conductivity. Data describing the resistivity are further discussed in the section of impedance spectroscopy. While single-layer graphene exhibits an enhanced electron transfer because of its sp<sup>2</sup> hybridized carbon atoms forming a  $\pi$ -conjugated system, fluorographene loses the conductivity with every carbon atom in sp<sup>3</sup> hybridization. It can be hypothesized that the contents of fluorine atoms as well as the number and type of defect play an important role in fluorographene chemistry. In order to understand the charge storage mechanism in detail, the electrode kinetic was studied. The total amount of charge stored in the electrode material is given by the combination of capacitive and intercalation effects. Apart from this, the capacitive process is composed of two different mechanisms: redox reaction and electric double-layer formation between the electrode/electrolyte interface (ion adsorption/desorption). According to the power law, the dependence of the scan rate on the current can be expressed by the following equation:

$$i = a\nu^b$$

where  $a$  and  $b$  are the adjustable parameters and  $\nu$  is the scan rate (V s<sup>-1</sup>).<sup>86</sup> When  $\log i$  is plotted against  $\log \nu$  at a fixed potential, the value of  $b$  can be obtained from the slope of a linear fit. In general, the  $b$ -factor has two states like  $b = 0.5$  referring to the diffusion-controlled intercalation process of ions into the electrode material (when the system satisfies Cottrell's equation, then:  $i = a\nu^{1/2}$ ) or  $b = 1$  for surface capacitive contribution or non-diffusive processes ( $i = a\nu$ ).<sup>87</sup> Fig. S2† represents plot  $\log i$  vs.  $\log \nu$  at different potentials, and Fig. 4e shows that the obtained  $b$ -factor is close to 1 at particular potentials. This evidences that the capacitive contribution prevails throughout the intercalation process.

The capacitive performance was further investigated using a galvanostatic charge/discharge (GCD) technique, as shown in Fig. 5a. It is worth noting that GCD can illustrate either EDLC or pseudo-capacitive behaviour as well as the internal resistance of the tested materials. Its application has then paramount importance for the testing of supercapacitors. As can be seen, the GCD profiles of the FG samples exhibit an almost symmetrical charge-discharge shape without obvious redox waves, indicating good capacitive performance. Linear GCD profiles also confirm that the TRFG samples could be regarded as EDLC. Fig. 5b displays the trend of specific capacitance

( $C_{sp}$ ) evolution in time for the synthesis of the TRFG samples (the data were recorded at a constant current density of 1 A g<sup>-1</sup>). Evidently, the maximum of specific capacity was reached after 20 hours of synthesis, giving the value of  $C_{sp}$  300 F g<sup>-1</sup>. Then, the  $C_{sp}$  dropped down up to 150 F g<sup>-1</sup>. This trend reflects the results obtained by means of cyclic voltammetry and could be attributed to the variation of sp<sup>2</sup>/sp<sup>3</sup> carbon, as described previously. Subsequently, the sample labelled FG-20H was selected as the best candidate for further evaluation. Fig. 5c demonstrates the GCD curves of GCEs modified with the FG-20H sample recorded at different current densities ranging from 0.25 A g<sup>-1</sup> to 5 A g<sup>-1</sup>. As is evident, all spectra remain almost symmetrical even at low current densities, implying a good capacitive behaviour. Fig. 5d shows the corresponding trend of  $C_{sp}$  evolution in time for the sample labelled FG-20H. It is obvious that the maximum of  $C_{sp}$  (539 F g<sup>-1</sup>) was reached at the current density of 0.25 A g<sup>-1</sup>. Such a value is higher than those previously reported for other carbon-based electrode materials measured under the same conditions.<sup>88–90</sup> Subsequently, it is possible to recognize a typical decrease in capacitance, giving the value of  $C_{sp}$  230 F g<sup>-1</sup> at 5 A g<sup>-1</sup>. Fig. 5e depicts a contour plot as a function of  $C_{sp}$  (F g<sup>-1</sup>) for all the synthesized samples at current densities ranging from 0.25 to 5 A g<sup>-1</sup>. The maximum of  $C_{sp}$  perfectly reflects all the results mentioned above. The life-time (cycling stability) of the FG-20H sample was also evaluated, as depicted in Fig. 5f. We found that  $C_{sp}$  remains perfectly stable for 1500 cycles in a three electrode setup, indicating that the FG-20H sample can be used as a suitable candidate for supercapacitor fabrication. We have also employed a two-electrode cell in order to prove the statement about the practical applicability of the FG-20H sample. Fig. S4a† shows that the tested sample was stable for 30 000 charging/discharging cycles with a capacitance retention of 96.7%. As shown in Fig. S4b–d,† two cells connected in series were also able to continuously power a red LED diode without obvious fading.

In order to gain a better insight into the electrochemical performance of fluorographene derivatives, we used the method of electrochemical impedance spectroscopy (EIS). The recorded spectra in the form of Nyquist plots (Fig. 6a) were analyzed using an equivalent circuit, as shown in Fig. 6b. As can be seen, in a high-frequency region ( $f < 1.2$  kHz), none of the spectra exhibit a semicircle responsible for the charge-transfer resistance,  $R_{ct}$ , indicating the good conductivity of the tested samples. It is well known that a microporous structure enables a fast ion exchange which can cause a decrease in  $R_{ct}$ .<sup>91,92</sup> Furthermore, the presence of the semi-ionic C–F bond can also positively influence the electronic conductivity, as previously published.<sup>66</sup> Apart from this, the presence of the semicircle is also connected with the faradaic reaction taking place at the electrode|electrolyte interface. On the basis of this evidence, we can conclude that all the tested materials can be considered EDLC supercapacitors. Furthermore, all the impedance spectra reveal a vertical line in the low-frequency region, which signifies a good diffusive behaviour of the electrolyte ions in the system. The slope of the  $\sim 45^\circ$  line (medium fre-



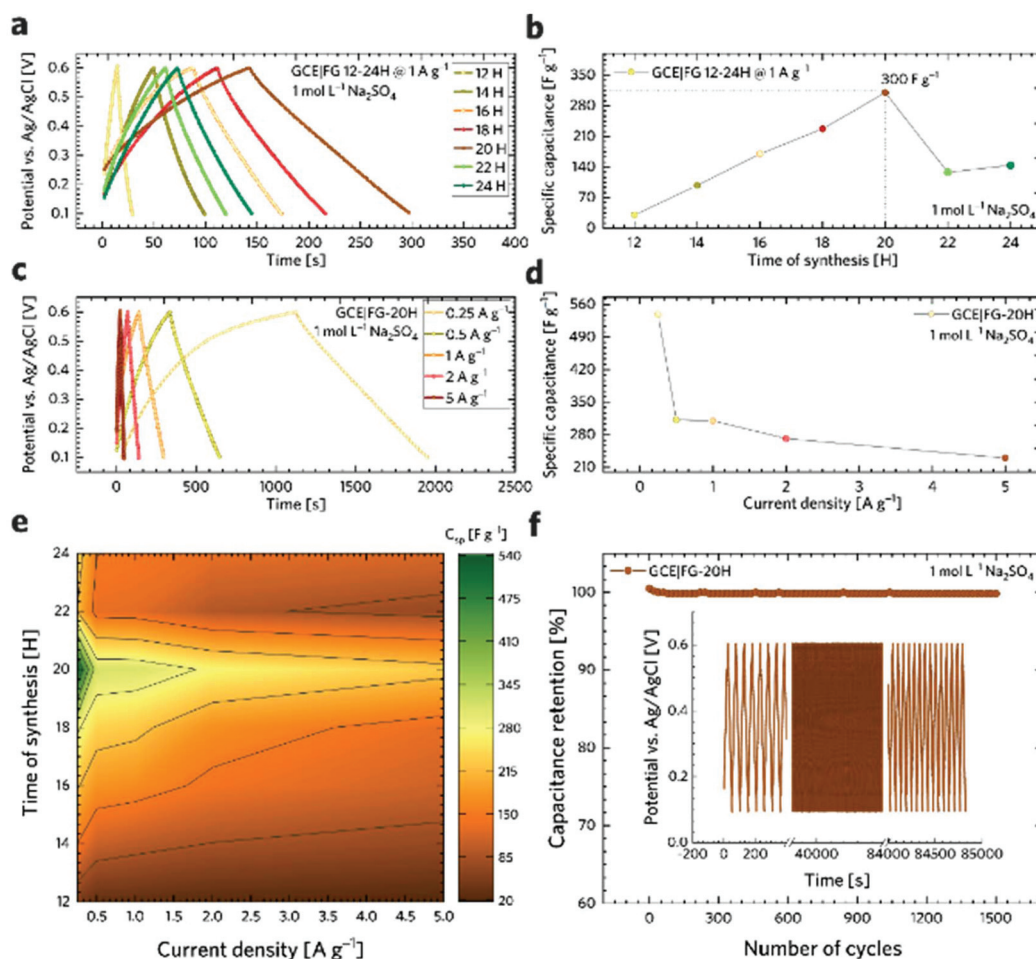


**Fig. 5** (a) Galvanostatic charge–discharge (GCD) profiles of GCEs modified with fluorographene samples prepared at a constant temperature of 450 °C at different times. (b) The trend of specific capacitance evolution in time during the FG sample synthesis. (c) The GCD curves of the FG-20H sample at different current densities ranging from 0.25 to 5 A g<sup>−1</sup>. (d) The change of specific capacitance of the FG-20H sample with increasing current density, (e) the contour plot of specific capacitance evolution in time of the FG sample recorded at different current densities. (f) Cycling stability of the FG-20H sample. All measurements were performed in 1 M Na<sub>2</sub>SO<sub>4</sub> aqueous electrolyte.

quency region;  $f < 1.32$  Hz) describes the diffusion of ions from the electrolyte into the electrode interface, corresponding to the Warburg impedance.<sup>93,94</sup> An almost linear vertical line in the Nyquist plot (low-frequency region,  $f < 0.5$  Hz) indicates a good capacitive behaviour. Since the vertical line of the sample FG-20H is more parallel to the y-axis, it can be concluded that the capacitance of this sample should be higher with respect to the others. The fitted data exhibit  $R_{ct}$  values with a decreasing trend ranging from 47.1  $\Omega$  (FG-12H) to 4.7  $\Omega$  (FG-20H), indicating an enhanced electron transfer. Furthermore, it is possible to observe an increase in the charge-transfer resistivity for the materials labelled FG-22H (24.9  $\Omega$ ) and FG-24H (40.1  $\Omega$ ), as shown in Fig. 6c. The trend of increasing resistivity could be related to the increase in the carbon atom content during the thermal decomposition of the fluorographene samples, which changes the type of defect responsible for the conductivity, as mentioned previously in a discussion concerning Raman spectroscopy. We also employed the Bode analysis in order to extract more details from the

impedance spectra of the FG-20H sample. As can be seen in Fig. 6d, the phase angle is close to the zero at high frequencies (orange region), indicating mostly resistive properties. When the frequency decreases, the phase angle reflects a more capacitive behaviour (blue region; phase angle  $-45^\circ$ ) until reaching fully capacitive response in the mHz region (green region, phase angle  $-76^\circ$ ). It is worth noting that this value is close to  $-90^\circ$ , which is typical of an ideal capacitor.<sup>95</sup> The frequency at  $-45^\circ$  should be also regarded as a point where the resistive and capacitive contribution is equal. The time constant (taken at the  $-45^\circ$  phase angle) is the time necessary for discharging the tested material with an efficiency of 63%, and can be expressed as follows:<sup>96</sup>

$$\tau_0 = \frac{1}{2\pi f_0}$$

Using this formula, the time constant was calculated to be 11.4 ms. This value is very promising compared to previously





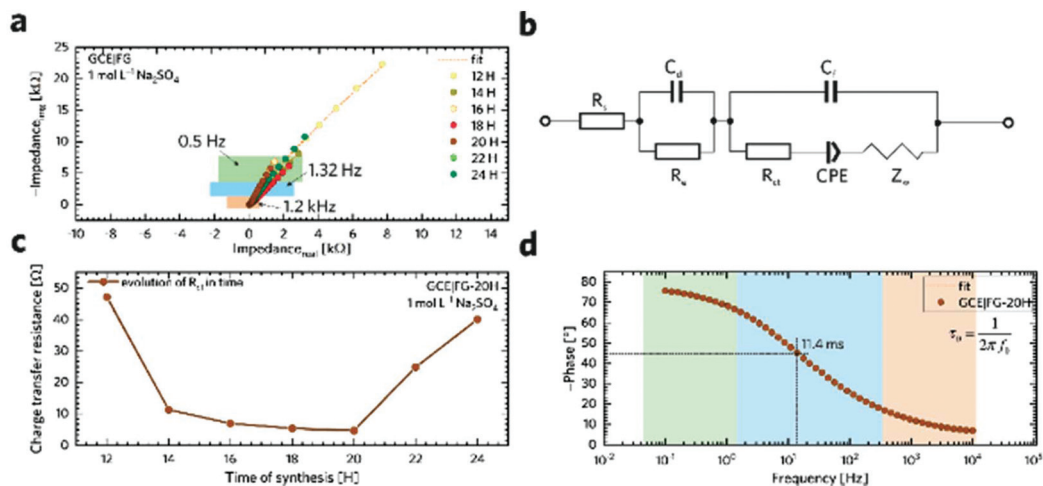
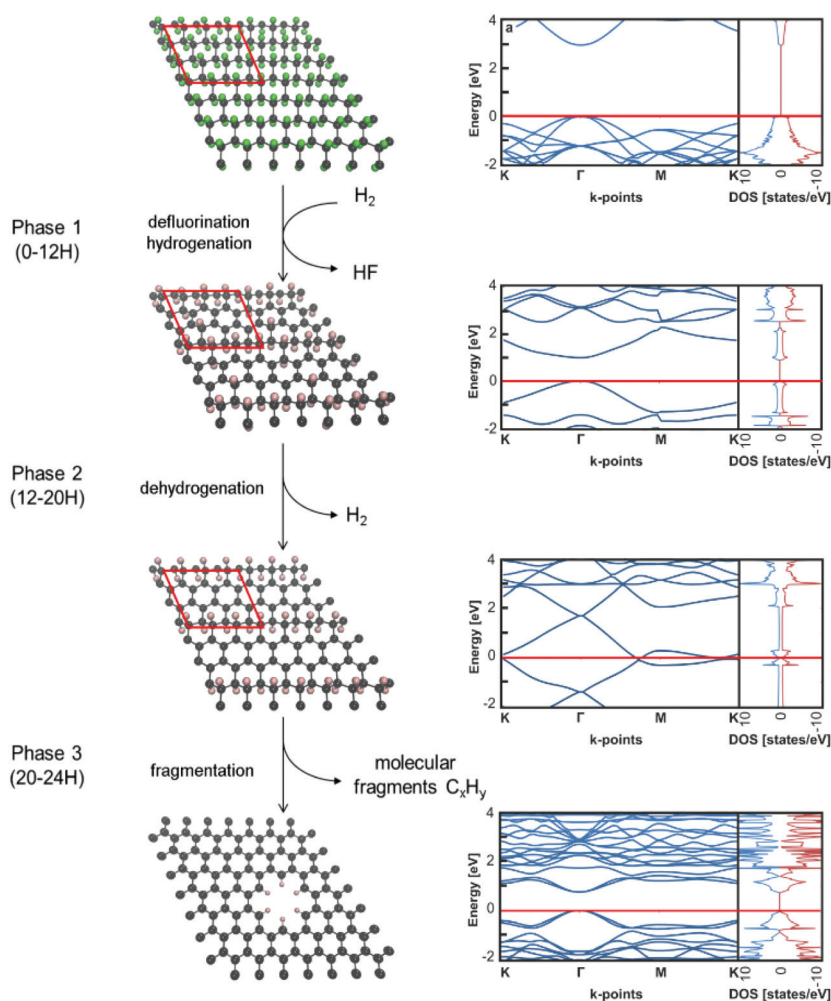


**Fig. 6** (a) Nyquist plots of GCEs modified with fluorographene samples prepared at a constant temperature of 450 °C for different times recorded in a frequency range from 0.01 Hz to 10 kHz at an open circuit potential (OCP) with 5 mV amplitude. (b) Modified Randles circuit used for data fitting. (c) The trend of  $R_{ct}$  change in time during the FG sample synthesis. (d) Bode representation of the FG-20H sample. All measurements were performed in 1 M  $\text{Na}_2\text{SO}_4$  aqueous electrolyte.



**Scheme 1** Proposed mechanism of defluorination of the fluorographene sample under a reducing hydrogen atmosphere. The Fermi level in the band structure and DOS (states per eV per computational cell) is set to zero.



published results for carbon derivatives such as carbon onions.<sup>97,98</sup> These results strongly suggest that fluorographene holds great potential as a material for supercapacitors.

### Computational insights into the reaction mechanism and structure–property relationships

To rationalize experimental observations occurring during the reaction, the following mechanism can be proposed (Scheme 1). In the first phase (0–12H), defluorination under the hydrogen atmosphere is accompanied by the binding of the atomic hydrogen (produced by a side reaction of released fluorine atoms with hydrogen molecules) to the lattice. The presence of hydrogen ad-atoms is in line with a relatively high proportion of  $sp^3$  carbon atoms in the FG-12H sample. During the second phase (12–20H), the material is stabilized by a thermodynamically favourable release of hydrogen, which increases the number of  $sp^2$  carbon atoms on the lattice. Fig. S5–S7† show that this process leads to the decrease in the band gaps in agreement with the increase of the specific capacitance and decrease of the charge transfer resistance. The final phase (20–24H) is apparently connected with the disruption of the material by releasing hydrogenated/fluorinated molecular fragments reflected in the increased porosity of the material. Feasibility of the fragmentation in the final phase is demonstrated by negative reaction energies for the release of  $C_6H_6$  and  $C_6H_{12}$  fragments (Fig. S8†). The evolution of electrochemical properties might also be related to a decrease in the fluorine concentration during the second and third phase of the reaction (Table 1). To address this issue, we analyzed the band structure of various heavily defluorinated structures (see the ESI†). We found that the migration of F ad-atoms over the lattice was feasible (the energy barrier is *ca.* 0.87–1.05 eV) and the topology of ad-atoms can indeed significantly affect the band structure of the material (Fig. S9 and S10†). However, this mechanism on its own does not satisfactorily explain the relatively high ratio of  $sp^3/sp^2$  carbon atoms in heavily defluorinated samples and its variations in the second phase of the reaction. To sum up, although the changes in the content and topology of F ad-atoms can contribute to altering the electric behavior of the samples, our calculations strongly support the above-described mechanism as the main reaction pathway, which is consistent with the experimental observations.

## Conclusions

In summary, a new way of synthesis of fluorographene derivatives was developed employing a method of thermal decomposition of a fully fluorinated sample in the presence of a reducing hydrogen atmosphere. Our results demonstrate that the number of fluorine atoms attached to the surface of graphene can be easily controlled by changing time at a constant temperature of 450 °C. We have shown that the capacitance is influenced by both the number of fluorine atoms and the hydrogenation process. An optimized material exhibits values of specific capacitance up to 539 F  $g^{-1}$  recorded at a current

density of 0.25 A  $g^{-1}$ . The optimized material can be cycled reversibly in the voltage range of 0.1–0.6 V and exhibits excellent cycling durability, with 100% specific capacitance retention after 1500 cycles in a three-electrode configuration and 96.7% specific capacitance after 30 000 cycles in a two-electrode setup. Moreover, a mechanism for charge storage was explained in detail using both experimental and theoretical approaches. The environmentally friendly nature of our derivatives (one-step synthesis without any presence of heavy metals, neutral character of the electrolyte) holds great potential in developing new kinds of supercapacitors for practical applications.

## Conflicts of interest

There are no conflicts to declare.

## Acknowledgements

The authors gratefully acknowledge the support by the Operational Programme Research, Development and Education - European Regional Development Fund, project no. CZ.02.1.01/0.0/0.0/16\_019/0000754 and CZ.02.1.01/0.0/0.0/15\_003/0000416 of the Ministry of Education, Youth and Sports of the Czech Republic. The authors also gratefully acknowledge the financial support from an ERC Consolidator Grant (H2020) No. 683024 and the student project IGA\_PrF\_2019\_031. We thank Ondřej Tomanec, Jana Stráská and Dr Eirini Ioannou, for HRTEM, TEM + SAED and SEM measurements.

## References

- 1 N. S. Lewis and D. G. Nocera, *Proc. Natl. Acad. Sci. U. S. A.*, 2006, **103**, 15729–15735.
- 2 L. Dai, D. W. Chang, J.-B. Baek and W. Lu, *Small*, 2012, **8**, 1130–1166.
- 3 A. S. Arico, P. Bruce, B. Scrosati, J. M. Tarascon and W. Van Schalkwijk, *Nat. Mater.*, 2005, **4**, 366–377.
- 4 J. Zhang, J. Jiang, H. Li and X. S. Zhao, *Energy Environ. Sci.*, 2011, **4**, 4009.
- 5 F. Béguin, V. Presser, A. Balducci and E. Frackowiak, *Adv. Mater.*, 2014, **26**, 2219–2251.
- 6 G. Wang, L. Zhang and J. Zhang, *Chem. Soc. Rev.*, 2012, **41**, 797–828.
- 7 G. Yu, X. Xie, L. Pan, Z. Bao and Y. Cui, *Nano Energy*, 2013, **2**, 213–234.
- 8 P. J. Hall, M. Mirzaei, S. I. Fletcher, F. B. Sillars, A. J. R. Rennie, G. O. Shitta-Bey, G. Wilson, A. Cruden and R. Carter, *Energy Environ. Sci.*, 2010, **3**, 1238.
- 9 X. Lang, A. Hirata, T. Fujita and M. Chen, *Nat. Nanotechnol.*, 2011, **6**, 232–236.
- 10 M. Zhi, C. Xiang, J. Li, M. Li and N. Wu, *Nanoscale*, 2013, **5**, 72–88.



- 11 V. Augustyn, P. Simon and B. Dunn, *Energy Environ. Sci.*, 2014, **7**, 1597.
- 12 E. Frackowiak, V. Khomenko, K. Jurewicz, K. Lota and F. Béguin, *J. Power Sources*, 2006, **153**, 413–418.
- 13 Z. Song and H. Zhou, *Energy Environ. Sci.*, 2013, **6**, 2280.
- 14 G. A. Snook, P. Kao and A. S. Best, *J. Power Sources*, 2011, **196**, 1–12.
- 15 J. Jiang, Y. Li, J. Liu, X. Huang, C. Yuan and X. W. D. Lou, *Adv. Mater.*, 2012, **24**, 5166–5180.
- 16 M. Toupin, T. Brousse and D. Bélanger, *Chem. Mater.*, 2004, **16**, 3184–3190.
- 17 D. Kong, J. Luo, Y. Wang, W. Ren, T. Yu, Y. Luo, Y. Yang and C. Cheng, *Adv. Funct. Mater.*, 2014, **24**, 3815–3826.
- 18 B. E. Conway, *Electrochemical Supercapacitors Scientific Fundamentals and Technological Applications*, Springer US, 1st edn, 1999.
- 19 G. Wang, H. Wang, X. Lu, Y. Ling, M. Yu, T. Zhai, Y. Tong and Y. Li, *Adv. Mater.*, 2014, **26**, 2676–2682.
- 20 J. Gamby, P. L. Taberna, P. Simon, J. F. Fauvarque and M. Chesneau, *J. Power Sources*, 2001, **101**, 109–116.
- 21 B. Li, F. Dai, Q. Xiao, L. Yang, J. Shen, C. Zhang and M. Cai, *Adv. Energy Mater.*, 2016, **6**, 1600802.
- 22 M. F. L. De Volder, S. H. Tawfick, R. H. Baughman and A. J. Hart, *Science*, 2013, **339**, 535–539.
- 23 Z. Niu, W. Zhou, X. Chen, J. Chen and S. Xie, *Adv. Mater.*, 2015, **27**, 6002–6008.
- 24 C. Fu, A. Mahadevegowda and P. S. Grant, *J. Mater. Chem. A*, 2015, **3**, 14245–14253.
- 25 C. Merino, P. Soto, E. Vilaplana-Ortego, J. M. Gomez de Salazar, F. Pico and J. M. Rojo, *Carbon*, 2005, **43**, 551–557.
- 26 C. Young, T. Park, J. W. Yi, J. Kim, Md. S. A. Hossain, Y. V. Kaneti and Y. Yamauchi, *ChemSusChem*, 2018, **11**, 3546–3558.
- 27 X. Xu, J. Zhou, D. H. Nagaraju, L. Jiang, V. R. Marinov, G. Lubineau, H. N. Alshareef and M. Oh, *Adv. Funct. Mater.*, 2015, **25**, 3193–3202.
- 28 P. Hao, Z. Zhao, Y. Leng, J. Tian, Y. Sang, R. I. Boughton, C. P. Wong, H. Liu and B. Yang, *Nano Energy*, 2015, **15**, 9–23.
- 29 G. Zu, J. Shen, L. Zou, F. Wang, X. Wang, Y. Zhang and X. Yao, *Carbon*, 2016, **99**, 203–211.
- 30 X. Wei, S. Wan and S. Gao, *Nano Energy*, 2016, **28**, 206–215.
- 31 X.-L. Wu, T. Wen, H.-L. Guo, S. Yang, X. Wang and A.-W. Xu, *ACS Nano*, 2013, **7**, 3589–3597.
- 32 M. Oschatz, S. Boukhalifa, W. Nickel, J. P. Hofmann, C. Fischer, G. Yushin and S. Kaskel, *Carbon*, 2017, **113**, 283–291.
- 33 V. Presser, M. Heon and Y. Gogotsi, *Adv. Funct. Mater.*, 2011, **21**, 810–833.
- 34 H. Su, H. Huang, H. Zhang, X. Chu, B. Zhang, B. Gu, X. Zheng, S. Wu, W. He, C. Yan, J. Chen and W. Yang, *ACS Appl. Energy Mater.*, 2018, **1**, 3544–3553.
- 35 L. Dai, *Acc. Chem. Res.*, 2013, **46**, 31–42.
- 36 Y. Wang, Z. Shi, Y. Huang, Y. Ma, C. Wang, M. Chen and Y. Chen, *J. Phys. Chem. C*, 2009, **113**, 13103–13107.
- 37 T. Kuila, S. Bose, A. K. Mishra, P. Khanra, N. H. Kim and J. H. Lee, *Prog. Mater. Sci.*, 2012, **57**, 1061–1105.
- 38 Y. Wang, Y. Wu, Y. Huang, F. Zhang, X. Yang, Y. Ma and Y. Chen, *J. Phys. Chem. C*, 2011, **115**, 23192–23197.
- 39 H. Jiang, P. S. Lee and C. Li, *Energy Environ. Sci.*, 2013, **6**, 41–53.
- 40 S. Han, D. Wu, S. Li, F. Zhang and X. Feng, *Adv. Mater.*, 2014, **26**, 849–864.
- 41 L. Qie, W. Chen, H. Xu, X. Xiong, Y. Jiang, F. Zou, X. Hu, Y. Xin, Z. Zhang and Y. Huang, *Energy Environ. Sci.*, 2013, **6**, 2497.
- 42 A. Borenstein, O. Hanna, R. Attias, S. Luski, T. Brousse and D. Aurbach, *J. Mater. Chem. A*, 2017, **5**, 12653–12672.
- 43 X. Yu, Y. Kang and H. S. Park, *Carbon*, 2016, **101**, 49–56.
- 44 N. Parveen, M. O. Ansari, S. A. Ansari and M. H. Cho, *J. Mater. Chem. A*, 2016, **4**, 233–240.
- 45 P. Chen, J.-J. Yang, S.-S. Li, Z. Wang, T.-Y. Xiao, Y.-H. Qian and S.-H. Yu, *Nano Energy*, 2013, **2**, 249–256.
- 46 Z.-S. Wu, G. Zhou, L.-C. Yin, W. Ren, F. Li and H.-M. Cheng, *Nano Energy*, 2012, **1**, 107–131.
- 47 Y. Zhang, L. Li, H. Su, W. Huang and X. Dong, *J. Mater. Chem. A*, 2015, **3**, 43–59.
- 48 Y. Yan, B. Li, W. Guo, H. Pang and H. Xue, *J. Power Sources*, 2016, **329**, 148–169.
- 49 P. Pachfule, D. Shinde, M. Majumder and Q. Xu, *Nat. Chem.*, 2016, **8**, 718–724.
- 50 W. Xia, C. Qu, Z. Liang, B. Zhao, S. Dai, B. Qiu, Y. Jiao, Q. Zhang, X. Huang, W. Guo, D. Dang, R. Zou, D. Xia, Q. Xu and M. Liu, *Nano Lett.*, 2017, **17**, 2788–2795.
- 51 X. Cao, B. Zheng, X. Rui, W. Shi, Q. Yan and H. Zhang, *Angew. Chem., Int. Ed.*, 2014, **53**, 1404–1409.
- 52 Y. Yan, P. Gu, S. Zheng, M. Zheng, H. Pang and H. Xue, *J. Mater. Chem. A*, 2016, **4**, 19078–19085.
- 53 Y. Yan, Y. Luo, J. Ma, B. Li, H. Xue and H. Pang, *Small*, 2018, **14**, 1801815.
- 54 Y. Xu, B. Li, S. Zheng, P. Wu, J. Zhan, H. Xue, Q. Xu and H. Pang, *J. Mater. Chem. A*, 2018, **6**, 22070–22076.
- 55 V. Georgakilas, M. Otyepka, A. B. Bourlinos, V. Chandra, N. Kim, K. C. Kemp, P. Hobza, R. Zboril and K. S. Kim, *Chem. Rev.*, 2012, **112**, 6156–6214.
- 56 D. D. Chronopoulos, A. Bakandritsos, M. Pykal, R. Zboril and M. Otyepka, *Appl. Mater. Today*, 2017, **9**, 60–70.
- 57 V. Georgakilas, J. N. Tiwari, K. C. Kemp, J. A. Perman, A. B. Bourlinos, K. S. Kim and R. Zboril, *Chem. Rev.*, 2016, **116**, 5464–5519.
- 58 H. L. Poh, P. Šimek, Z. Sofer and M. Pumera, *Chem. – Eur. J.*, 2013, **19**, 2655–2662.
- 59 E. Widenkvist, D. W. Boukhvalov, S. Rubino, S. Akhtar, J. Lu, R. A. Quinlan, M. I. Katsnelson, K. Leifer, H. Grennberg and U. Jansson, *J. Phys. D: Appl. Phys.*, 2009, **42**, 112003.
- 60 J. Zhou, J. Lian, L. Hou, J. Zhang, H. Gou, M. Xia, Y. Zhao, T. A. Strobel, L. Tao and F. Gao, *Nat. Commun.*, 2015, **6**, 8503.





- 61 Y. Zhu, H. Cui, X. Meng, J. Zheng, P. Yang, L. Li, Z. Wang, S. Jia and Z. Zhu, *ACS Appl. Mater. Interfaces*, 2016, **8**, 6481–6487.
- 62 F. Karlický, K. Kumara Ramanatha Datta, M. Otyepka and R. Zbořil, *ACS Nano*, 2013, **7**, 6434–6464.
- 63 Z. Kou, B. Guo, Y. Zhao, S. Huang, T. Meng, J. Zhang, W. Li, I. S. Amiinu, Z. Pu, M. Wang, M. Jiang, X. Liu, Y. Tang and S. Mu, *ACS Appl. Mater. Interfaces*, 2017, **9**, 3702–3712.
- 64 K. Kakaei, M. Hamidi and S. Husseindoost, *J. Colloid Interface Sci.*, 2016, **479**, 121–126.
- 65 X. Ye, Y. Zhu, H. Jiang, L. Wang, P. Zhao, Z. Yue, Z. Wan and C. Jia, *Chem. Eng. J.*, 2019, **361**, 1437–1450.
- 66 H. An, Y. Li, P. Long, Y. Gao, C. Qin, C. Cao, Y. Feng and W. Feng, *J. Power Sources*, 2016, **312**, 146–155.
- 67 L. G. Bulusheva, V. A. Tur, E. O. Fedorovskaya, I. P. Asanov, D. Pontiroli, M. Riccò and A. V. Okotrub, *Carbon*, 2014, **78**, 137–146.
- 68 J. Rouquerol, F. Rouquerol, P. Llewellyn, G. Maurin and K. S. W. Sing, *Adsorption by Powders and Porous Solids: Principles, Methodology and Applications*, Elsevier Science, 2013.
- 69 J. P. Perdew, K. Burke and M. Ernzerhof, *Phys. Rev. Lett.*, 1996, **77**, 3865–3868.
- 70 P. E. Blöchl, *Phys. Rev. B: Condens. Matter Mater. Phys.*, 1994, **50**, 17953–17979.
- 71 G. Kresse and D. Joubert, *Phys. Rev. B: Condens. Matter Mater. Phys.*, 1999, **59**, 1758–1775.
- 72 G. Kresse and J. Furthmüller, *Phys. Rev. B: Condens. Matter Mater. Phys.*, 1996, **54**, 11169–11186.
- 73 G. Kresse and J. Furthmüller, *Comput. Mater. Sci.*, 1996, **6**, 15–50.
- 74 H. J. Monkhorst and J. D. Pack, *Phys. Rev. B: Solid State*, 1976, **13**, 5188–5192.
- 75 A. Gupta, G. Chen, P. Joshi, S. Tadigadapa and P. C. Eklund, *Nano Lett.*, 2006, **6**, 2667–2673.
- 76 A. C. Ferrari, *Solid State Commun.*, 2007, **143**, 47–57.
- 77 A. C. Ferrari, J. C. Meyer, V. Scardaci, C. Casiraghi, M. Lazzeri, F. Mauri, S. Piscanec, D. Jiang, K. S. Novoselov, S. Roth and A. K. Geim, *Phys. Rev. Lett.*, 2006, **97**(18), 187401.
- 78 A. Eckmann, A. Felten, A. Mishchenko, L. Britnell, R. Krupke, K. S. Novoselov and C. Casiraghi, *Nano Lett.*, 2012, **12**, 3925–3930.
- 79 M. Herraiz, M. Dubois, N. Batisse, S. Hajjar-Garreau and L. Simon, *Dalton Trans.*, 2018, **47**, 4596–4606.
- 80 M. Dubois, K. Guérin, Y. Ahmad, N. Batisse, M. Mar, L. Frezet, W. Hourani, J.-L. Bubendorff, J. Parmentier, S. Hajjar-Garreau and L. Simon, *Carbon*, 2014, **77**, 688–704.
- 81 W. Lai, D. Xu, X. Wang, Z. Wang, Y. Liu, X. Zhang and X. Liu, *Phys. Chem. Chem. Phys.*, 2017, **19**, 19442–19451.
- 82 C. Sun, Y. Feng, Y. Li, C. Qin, Q. Zhang and W. Feng, *Nanoscale*, 2014, **6**, 2634–2641.
- 83 X. Yin, Y. Feng, Q. Zhao, Y. Li, S. Li, H. Dong, W. Hu and W. Feng, *J. Mater. Chem. C*, 2018, **6**, 6378–6384.
- 84 R. R. Nair, W. Ren, R. Jalil, I. Riaz, V. G. Kravets, L. Britnell, P. Blake, F. Schedin, A. S. Mayorov, S. Yuan, M. I. Katsnelson, H. M. Cheng, W. Strupinski, L. G. Bulusheva, A. V. Okotrub, I. V. Grigorieva, A. N. Grigorenko, K. S. Novoselov and A. K. Geim, *Small*, 2010, **6**, 2877–2884.
- 85 W. Feng, P. Long, Y. Feng and Y. Li, *Adv. Sci.*, 2016, **3**, 1500413.
- 86 H. Lindström, S. Södergren, A. Solbrand, H. Rensmo, J. Hjelm, A. Hagfeldt and S.-E. Lindquist, *J. Phys. Chem. B*, 1997, **101**, 7717–7722.
- 87 J. Wang, J. Polleux, J. Lim and B. Dunn, *J. Phys. Chem. C*, 2007, **111**, 14925–14931.
- 88 S. Cho, K.-H. Shin and J. Jang, *ACS Appl. Mater. Interfaces*, 2013, **5**, 9186–9193.
- 89 K. Xia, Z. Huang, L. Zheng, B. Han, Q. Gao, C. Zhou, H. Wang and J. Wu, *J. Power Sources*, 2017, **365**, 380–388.
- 90 Z. Chen, L. Hou, Y. Cao, Y. Tang and Y. Li, *Appl. Surf. Sci.*, 2018, **435**, 937–944.
- 91 C. Largeot, C. Portet, J. Chmiola, P.-L. Taberna, Y. Gogotsi and P. Simon, *J. Am. Chem. Soc.*, 2008, **130**, 2730–2731.
- 92 R. K. Kalluri, M. M. Biener, M. E. Suss, M. D. Merrill, M. Stadermann, J. G. Santiago, T. F. Baumann, J. Biener and A. Striolo, *Phys. Chem. Chem. Phys.*, 2013, **15**, 2309.
- 93 M. Li, C. Liu, H. Cao, H. Zhao, Y. Zhang and Z. Fan, *J. Mater. Chem. A*, 2014, **2**, 14844.
- 94 S. Buller, M. Thele, R. W. A. A. DeDoncker and E. Karden, *IEEE Trans. Ind. Appl.*, 2005, **41**, 742–747.
- 95 J. Zhang and X. S. Zhao, *ChemSusChem*, 2012, **5**, 818–841.
- 96 A. Noori, M. F. El-Kady, M. S. Rahmanifar, R. B. Kaner and M. F. Mousavi, *Chem. Soc. Rev.*, 2019, **48**, 1272–1341.
- 97 D. Pech, M. Brunet, H. Durou, P. Huang, V. Mochalin, Y. Gogotsi, P.-L. Taberna and P. Simon, *Nat. Nanotechnol.*, 2010, **5**, 651–654.
- 98 B. Abdulhakeem, B. Farshad, M. Damilola, T. Fatemeh, F. Mopeli, D. Julien and M. Ncholu, *RSC Adv.*, 2014, **4**, 39066.

